ResearchGate

See discussions, stats, and author profiles for this publication at: https://www.researchgate.net/publication/271226787

Two-Dimensional Transition-Metal Electride Y2C

ARTICLE *in* CHEMISTRY OF MATERIALS · OCTOBER 2014

Impact Factor: 8.35 · DOI: 10.1021/cm503512h

CITATIONS
3

READS
57

8 AUTHORS, INCLUDING:

Zewen Xiao
University of Toledo

13 PUBLICATIONS **18** CITATIONS

SEE PROFILE

Hechang Lei
Tokyo Institute of Technology

131 PUBLICATIONS **1,055** CITATIONS

SEE PROFILE

Shigenori Ueda
National Institute for Materials Science

190 PUBLICATIONS **2,246** CITATIONS

SEE PROFILE

Available from: Zewen Xiao
Retrieved on: 24 January 2016

CHEMISTRY OF MATERIALS

Article

pubs.acs.org/cm

Two-Dimensional Transition-Metal Electride Y_2C

Xiao Zhang,[†,∇,¶] Zewen Xiao,[‡,¶] Hechang Lei,[†] Yoshitake Toda,[†,∇] Satoru Matsuishi,[†] Toshio Kamiya,[†,‡] Shigenori Ueda,[§] and Hideo Hosono*[,†,‡,∇]

[†]Materials Research Center for Element Strategy, Tokyo Institute of Technology, Yokohama 226-8503, Japan

[‡]Materials and Structures Laboratory, Tokyo Institute of Technology, Yokohama 226-8503, Japan

[§]Synchrotron X-ray Station at Spring-8, National Institute for Material Science (NIMS), Hyogo 679-5148, Japan

[∇]ACCEL Project, Japan Science and Technology Agency (JST), Tokyo 102-8666, Japan

ABSTRACT: Electrides are ionic crystals in which the anionic electrons are confined to interstitial subnanometer-sized spaces. At present, the reported electrides only consist of main-group elements. Here, we report a layered-structure transition-metal hypocarbide electride, Y_2C, with quasi-two-dimensional (quasi-2D) anionic electrons confined in the interlayer space. Physical properties measurements reveal polycrystalline Y_2C exhibits semimetallic behavior, and paramagnetism with an effective magnetic moment of ~0.6 μ_B/Y, because of the existence of localized d-electrons. Photoelectron spectroscopy measurements illustrate the work function of polycrystalline Y_2C is 2.9 eV, lower than Y metal, revealing the loosely bound nature of the anionic electrons. Density functional theory calculations indicate the density of states at the Fermi level originates from the states at interstitial sites and the Y 4d-orbitals, supporting the confinement of anionic electrons within the interlayer space. These results demonstrate that Y_2C is a quasi-2D electride in term of $[Y_2C]^{1.8+}\cdot 1.8e^-$, and the coexistence of the anionic electrons and the Y 4d-electrons leads to the semimetallic behavior.

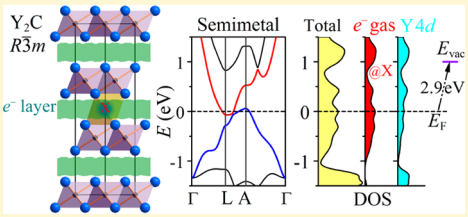

■ INTRODUCTION

Electrides are peculiar ionic crystals in which electrons serve as anions.[1,2] Distinct from the almost fully delocalized electrons in metals, the electrons in electrides do not belong to any particular atom, molecule, or bond and are confined in the cavities stoichiometrically and periodically. Because electrons have significantly smaller mass than anions, there is a pronounced quantum effect in these types of materials, and the loosely bound anionic electrons lead to unique properties, such as significantly high conductivity of various types,[1,3,4] low work function,[5] and high hyperpolarizabilities.[6] Since the discovery of the first crystalline organic electride, $Cs^+(18C6)_2\cdot e^-$, by Ellaboudy et al.,[7] seven organic electrides have been synthesized.[8] Because of the thermal instability of organic electrides, the applications of these materials are impeded. To improve the stability, inorganic electrides composed of inert inorganic framework were proposed;[9] finally the first room-temperature and air-stable inorganic electride, $[Ca_{24}Al_{28}O_{64}]^{4+}\cdot(4e^-)$, was realized in 2003,[3] having the unique properties of high electron conductivity, combined with low work function provided a broad range of application for the next generation of electronics. For example, it is a promising cathode material with a low electron-injection barrier for organic light-emitting diodes (OLEDs)[10] and it is also an efficient catalyst for ammonia synthesis.[11]

For all of these electrides, the topologies of the cavities confining the anionic electrons are zero-dimensional (0D, isolated cavities). This low dimensionality makes electrons difficult to delocalize, which limits the conductivity of these materials. Recently, the two-dimensional (2D) electride Ca_2N was reported.[12] Systematic characterization of the single-crystalline Ca_2N and theoretical calculation indicated that there is one anionic electron per Ca_2N unit cell ($[Ca_2N]^+\cdot e^-$), confined in the interlayer space. Surprisingly, the anionic electrons in Ca_2N are well-delocalized, which is significantly different from the reported electrides. This suggests that the dimensionality has a vital effect on the physical properties of the electride. On the other hand, until now, all of the known electrides consist of main group elements, i.e., the s-orbital plays an important role in their formation. Moreover, experimental and theoretical studies indicated that inorganic electrides can also form at very high pressures, and, again, all of the high-pressure electrides are still limited to main-group elements.[13−15] Because the formation of high-pressure electrides (HPEs) is dependent on the relative energy difference between certain orbital and interstitial quasi-atoms under pressure, and the energy slopes in various orbitals are different (s > p > d), HPEs are likely composed of the main-group elements (Li, Na, Al, Tl, etc.), but it is very difficult to form an electride from elements with valence d-electrons.[15] Therefore, exploration of new 2D electrides containing transition metals is important not only to applications but also to extend the concepts in condensed matter physics and solid-state chemistry.

Yttrium hypocarbide (Y_2C) is a typical rare-earth carbide with anti-$CdCl_2$ type structure and is isostructural to Ca_2N.

Received: September 23, 2014
Revised: October 21, 2014
Published: October 24, 2014

 © 2014 American Chemical Society

Recent *ab initio* calculations have predicted that Y_2C could be a 2D electride.[16] From the viewpoint of the standard valence states, there should be two excess electrons confined within the interlayer space, so the chemical formula can be described, approximately, as $[Y_2C]^{2+}\cdot 2e^-$. This is distinct from Ca_2N, in which only one electron well-delocalized in the interlayer space serves as the anionic electron. In order to confirm the theoretical prediction and clarify the physical properties of Y_2C, we synthesized polycrystalline Y_2C samples and studied the transport properties, examined the electronic structure by hard X-ray photoelectron spectroscopy (HAXPES), and determined the work function by UV photoelectron spectroscopy (UPS). Density functional theory (DFT) calculations were used to provide details about the electronic structure. All the results indicate that Y_2C is a quasi-2D electride with low work function. Most importantly, the valence d-electrons of Y have critical influence on the physical properties.

METHODS

Synthesis and Characterization. We synthesized polycrystalline Y_2C by arc melting under argon atmosphere on a water-cooled copper hearth with yttrium ingot (99.9%) shots and carbon granules (99.99%) in a molar ratio of 2:1. Pellets were flipped and remelted several times to ensure homogeneity. The as-grown polycrystalline Y_2C possesses a metallic luster and is brittle enough to be crushed into powders. It decomposes slowly in oxygen and moisture air, so all manipulations were performed in a purified argon-filled glovebox. The well-grounded powder sample was sealed in a plastic sample cell filled with argon gas and characterized by powder X-ray diffraction (pXRD), using a Bruker D8 Avance diffractometer with Cu Kα radiation at room temperature. Rietveld refinements of the data were performed with the TOPAS package.[17]

Transport Measurement. Resistivity, Hall resistivity, and specific heat measurements were performed by using a physical property measurement system (PPMS) (Quantum Design). The resistivity and Hall resistivity were measured by the four-wire method. The Hall resistivity was extracted from the difference of transverse resistance measured at the positive and negative field, i.e., $\rho_{xy}(H) = [\rho(H) + \rho(-H)]/2$, which can effectively eliminate the longitudinal resistivity component, because of voltage probe misalignment. The sample surfaces were lightly coated with grease (Apiezon-N) after contact fabrication to prevent the sample from reacting with ambient air during the measurement. The DC magnetic susceptibility measurements were conducted in a 10 kOe applied magnetic field using a vibrating sample magnetometer (VSM, Quantum Design).

Photoelectron Spectroscopy. Photoelectron spectroscopy measurements were performed with both the undulator beamline BL15XU of SPring-8 (HAXPES, $h\nu$ = 5950.2 eV)[18,19] and a He I discharge lamp light source (UPS, $h\nu$ = 21.2 eV) at room temperature, where the binding energy is measured from the Fermi energy (E_F), which is calibrated using a reference spectrum measured on a thin film of gold. The total energy resolutions for HAXPES and UPS were set to 240 and 200 meV, respectively. The base pressures of the HAXPES and UPS chamber attached to hemispherical electron analyzers (VG Scienta R4000 for HAXPES, Omicron EA125 for UPS) were better than 1×10^{-7} Pa and 2×10^{-8} Pa, respectively. In the UPS measurements, negative bias voltages up to 10 V were applied to the sample to guarantee that the vacuum level of the sample exceeds that of the electron analyzer. To prepare a clean Y_2C surface, the polycrystalline pellet was cleaved in a prepared chamber attached to the measurement chamber under 1×10^{-7} Pa.

DFT Calculations. DFT calculations were performed using the generalized gradient approximation (GGA) with the Perdew−Burke−Ernzerhof (PBE96)[20] functional and the projector augmented plane-wave method implemented in the Vienna *ab initio* simulation program (VASP 5.3).[21] A primitive rhombohedral unit cell was used for the electronic structure calculations. The plane wave cutoff energy was set to 500 eV. A 16 × 16 × 16 *k*-mesh was used for structural relaxation, and a 32 × 32 × 32 *k*-mesh was used for self-consistent and density of states (DOS) calculations. The Fermi surface was extracted from band energies from DOS calculations with 70 000 *k* points by WIEN2k[22] and visualized by XCrySDen.[23]. The electron-localized functional (ELF) was calculated to determine the bonding nature in Y_2C. The work function (Φ_{WF}) was determined for both the $(0001)_H$ and the $(11\bar{2}0)_H$ surfaces, based on a slab model. The slab supercell representing the $(0001)_H$ surface contained six hexagonal layers of M-X-M (18 atoms) and 20 Å of vacuum and that for the $(11\bar{2}0)_H$ surface contained 15 atom layers (45 atoms) and 20 Å of vacuum. A 15 × 15 × 1 Monkhorst−Pack *k*-point grid and a 7 × 7 × 1 Monkhorst−Pack *k*-point grid were used for the two surfaces, respectively. For all slabs, the middle one-third of atoms was fixed to serve as "bulk" and the outer two-thirds were relaxed to form the "surface". The Φ_{WF} value was determined using the equation

$$\Phi_{WF} = \phi_{vac}e - E_F$$

where ϕ_{vac} is the electrostatic potential of the vacuum region, and e is the charge of an electron.[24] Since the value of E_F cannot be accurately determined from a finite-slab calculation, it was obtained from a bulk calculation (E_F, bulk) and aligned with the equation

$$E_F = E_{F,bulk} - (\phi_{slab} - \phi_{bulk})e$$

where ϕ_{slab} and ϕ_{bulk} are the average potentials of the bulk and the "bulk" region of the slab, respectively.

RESULTS

Basic Properties of Y_2C. Figure 1 shows the pXRD pattern of Y_2C, which can be well-fitted by using the crystal structure

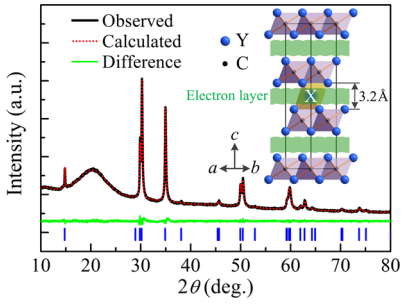

Figure 1. The powder X-ray diffraction (pXRD) pattern and Rietveld refinement of Y_2C. Plot shows the observed (solid black line) and calculated (dotted red line) pXRD patterns with a difference curve (solid green line). Vertical tick marks represent Bragg reflections in the $R\bar{3}m$ space group. The broad peak located at ∼20° originates from the diffraction of plastic cap of sample cell. Inset: Crystal structure of Y_2C in conventional hexagonal unit cell with Y sites marked in blue and C sites marked in black. The interstitial space (denoted by a white "X") is located at the center of the Y_6C octahedron.

reported in the literature.[17] The crystal structure of Y_2C (the inset of Figure 1) is an anti-$CdCl_2$ type structure with $R\bar{3}m$ space group that is isostructural to Ca_2N. The *a*- and *c*-axial lattice parameters obtained by Rietveld refinement are 3.6164(1) and 17.9651(6) Å, respectively, which are close to the reported values (a = 3.617 Å and c = 17.96 Å).[25] In this hexagonal layered structure, the edge-sharing Y_6C octahedra form a $[Y_2C]$ layer along the *ab*-plane, and this layer is stacked along the *c*-axis with an interlayer distance of ∼3.23 Å, which is much larger than the thickness (∼2.75 Å) of the $[Y_2C]$ layer unit. The interstitial position (as denoted by "X" in the inset of Figure 1) between the $[Y_2C]$ layers is located at the center of the Y_6C octahedron. The *a*-axial lattice parameter of Y_2C is similar to that of Ca_2N ($a \approx 3.63$ Å), and the *c*-axial is

significantly smaller than that of Ca_2N ($c \approx 19.13$ Å).[12] The $[Y_2C]$ layer unit can be regarded as a positively charged ionic slab and the interlayer spacing works as a confinement space for the anionic electrons at a stoichiometric composition. The shrinkage of the c-axial value indicates the remarkable increase of Coulombic attraction between the cationic layers and the anionic electrons at an interlayer space, which implies that more electrons are confined in the interlayer space than in Ca_2N.

Figure 2 shows the transport properties of polycrystalline Y_2C. The temperature dependence of resistivity $\rho(T)$ (Figure 2a) exhibits a metallic behavior with resistivity $\rho = 217$ $\mu\Omega$ cm at 300 K. The linear temperature dependence of $\rho(T)$ at high temperatures suggests that the electron phonon scattering is the dominant scattering mechanism in Y_2C. Furthermore, $\rho(T)$ at low temperatures ($2\ \mathrm{K} \leq T \leq 40$ K) can be well-fitted by the formula $\rho(T) = \rho(0) + AT^n$, with $n = 3.47(3)$, but not by Bloch–Grüneisen formula with $n = 5$, implying that interband s–d electron phonon scattering, rather than the intraband s–s electron phonon scattering is dominant at low temperatures. A similar behavior is observed in yttrium metal as well as in other transition metals.[26,27] The scattering processes observed in Y_2C are different from that in Ca_2N. The resistivity of Ca_2N tends toward the T^2 dependence expected for electron–electron scattering at low temperatures.

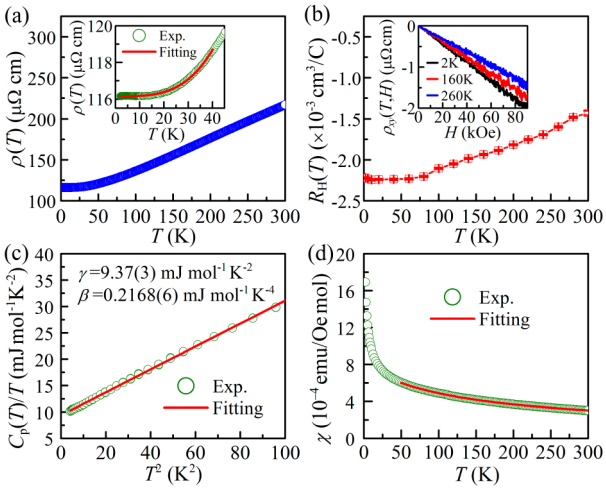

Figure 2. (a) Temperature dependence of the resistivity $\rho(T)$ for Y_2C (inset shows the enlarged part of the resistivity at low temperature; the solid line is the fitting result). (b) Temperature dependence of the Hall coefficient $R_H(T)$ (inset shows the magnetic field dependence of $\rho_{xy}(T,H)$ up to 90 kOe at T = 2, 160, and 260 K. (c) Specific heat divided by temperature $C_p(T)/T$ as a function of T^2 in low temperature region (blue open circles) (the solid line represents the fitting curve using the formula $C_p(T)/T = \gamma + \beta T^2$). (d) The magnetic susceptibility of Y_2C measured at 1 T, and the solid line represents the fitting curve using the formula $\chi = \chi_0 + C/(T - \Theta)$ in the temperature range of 50–300 K.

Hall effect measurements (Figure 2b) indicate the primary charge carrier is an electron and the Hall coefficient ($R_H(T)$) shows a remarkable temperature dependence. The carrier density (n_0) estimated assuming the free electron model ($R_H{}^0 = \rho_{xy}(T,H)/H = 1/n_0e$) is $4.37(8) \times 10^{21}$ cm^{-3} at 300 K, which is much smaller than the theoretical concentration of anionic electron ($\sim 2.94 \times 10^{22}$ cm^{-3}) based on the chemical formula of $[Y_2C]^{2+}\cdot 2e^-$ and even smaller than that in good metals, such as alkali metals and alkali-earth metals. According to the results of band structure calculation shown below, the Y_2C is a semimetal and the carrier concentrations in the two bands should be compensated. Therefore, according to ref 28, $R_H(T)$ can be defined as $R_H(T) = \rho_{xy}(T,H)/H = (1/n(T)e)[(\mu_e(T) - \mu_h(T))/(\mu_e(T) + \mu_h(T))]$, where $\mu_e(T)$ and $\mu_h(T)$ are mobilities in the electron and hole bands, respectively. Since $R_H(T)$ of Y_2C is negative, the mobility of the electron is greater than that of the hole ($\mu_e(T) - \mu_h(T) > 0$). On the other hand, because $[\mu_e(T) - \mu_h(T)]/[\mu_e(T) + \mu_h(T)] < 1$, the real carrier concentration n in Y_2C should be lower than n_0.

The specific heat at low temperatures is shown in Figure 2c. The data can be well-fitted by the expression $C_p(T)/T = \gamma + \beta T^2$. The derived Sommerfeld coefficient (γ) and the Debye temperature ($\Theta_D = (12\pi^4NR/5\beta)^{1/3}$) are ~9.37(3) mJ/mol K^2 and 299.6(3) K, respectively, where N is the number of atoms per formula unit (here, $N = 3$) and R is the gas constant. According to the formula $\gamma = \pi^2k_B{}^2N(E_F)/3$, where k_B is the Boltzmann constant, the estimated value of DOS at E_F ($N(E_F)$) is 3.95(4) states/eV per formula unit (f.u.). Using the free-electron model,

$$\gamma = k_B{}^2V(3\pi^2n_0)^{1/3}\frac{(m^*/h^2)}{3}$$

where V and m^* are the molar volume and effective mass, respectively, we have $m^* = 10.1(1)m_0$ (m_0 is the free electron mass) at 2K.

The magnetic properties of the polycrystalline Y_2C were assessed by plotting the magnetic susceptibility as a function of temperature under a magnetic field of 10 kOe (Figure 2d). The susceptibility curve (χ) shows typical paramagnetic behavior in the entire temperature range. Applying the modified Curie–Weiss law in the form $\chi = \chi_0 + C/(T - \Theta)$, where χ_0 is a temperature-independent term, Θ is the Curie–Weiss temperature and C is the Curie–Weiss constant. The χ_0 term was introduced into the Curie–Weiss law in order to account for free-electron susceptibility and diamagnetic susceptibility. The estimated χ_0 and Θ values are $8.9(2) \times 10^{-5}$ emu/mol Oe and $-129(2)$ K, respectively. A negative Weiss temperature was also observed in yttrium metal.[29] The calculated effective magnetic moment (μ_{eff}) is $0.604(4)\mu_B$/Y, clearly indicating that there is a localized moment in Y_2C.

Photoelectron Spectroscopy and Work Function. HAXPES is a powerful tool to investigate the bulk electronic properties of materials. The reduced surface sensitivity of the HAXPES technique relaxes stringent surface preparation requirements, thereby allowing the intrinsic electronic structure measurement of the as-grown sample. The top panel of Figure 3a depicts the valence band electronic structure of polycrystalline Y_2C measured by HAXPES, where a very clear Fermi edge reveals the metallic state of Y_2C, consistent with the transport measurement results. The general features, such as the hump structure around E_F and two peaks at 1.5 and 2.7 eV above E_F, are in agreement with the calculated total DOS, as shown in the bottom of Figure 3a.

The work function of polycrystalline Y_2C ($\Phi_{WF,poly}$) was determined from the cutoff of the secondary electron measured by UPS, as shown in Figure 3b. The $\Phi_{WF,poly}$ was determined to be 2.9 ± 0.1 eV. The valence band UPS spectrum (the inset of Figure 3b) is similar to the valence band HAXPES spectrum. Figures 3c and 3d show the calculated potential energies (ϕe) averaged over the $(0001)_H$ and the $(11\bar{2}0)_H$ planes based on DFT, from which the $\Phi_{WF,theory}$ for the $(0001)_H$ and the

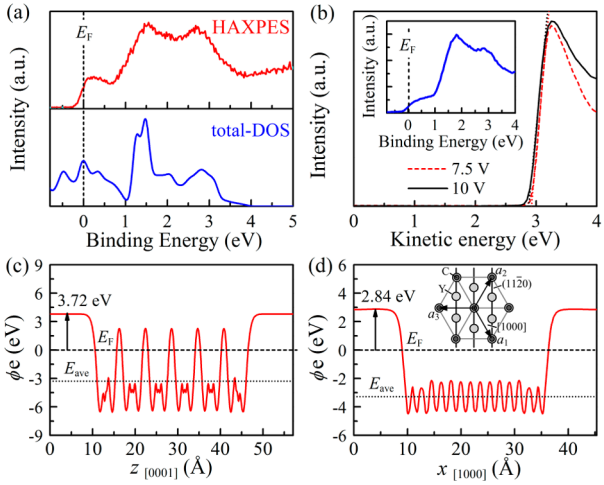

Figure 3. (a) Valence-band HAXPES spectrum for the polycrystalline Y_2C sample (upper panel) and calculated total DOS of Y_2C (lower panel). (b) UPS spectra of the polycrystalline Y_2C sample measured at different bias voltages to detect the work function. Inset shows the valence-band UPS spectrum for the polycrystalline Y_2C. Potentials (relative to E_F, eV) averaged over the (c) $(0001)_H$ surface (panel c) and (d) $(11\bar{2}0)_H$ surface (panel d), as a function of position (Å). The blue horizontal lines refer to the average bulk potential. The inset of panel (d) shows a top view of the $(0001)_H$ and $(11\bar{2}0)_H$ surfaces, represented using a four-axis coordinate system.

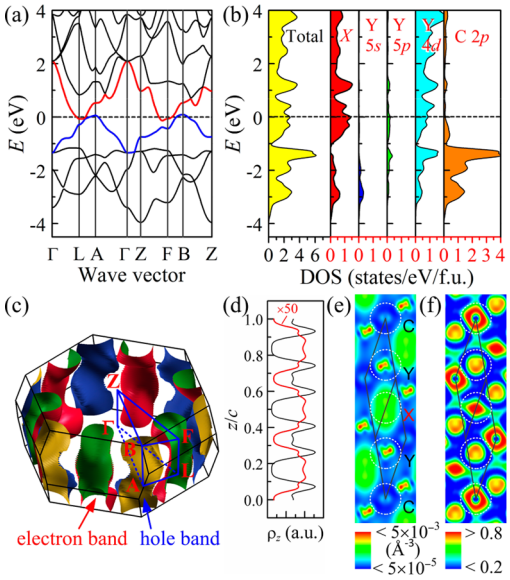

Figure 4. (a) Band dispersion of Y_2C along the high symmetry lines (the dashed line indicates the Fermi level, and the bands in blue and red represent the hole-like and electron-like bands, respectively). (b) Total and projected DOSs of Y_2C. (c) Fermi surfaces in the first Brillouin zone. (d) The averaged total valence electron density (black line) and projected electron density (red line) along the c-axis for the room-temperature (k_BT) region near E_F. (e) Electron density maps. (f) Electron-localized functional (ELF) on the $(11\bar{2}0)_H$ plane.

$(11\bar{2}0)_H$ surfaces were determined to be 3.72 and 2.84 eV, respectively. The large difference of $\Phi_{WF,theory}$ (0.88 eV) between these surfaces reflects the highly anisotropic character of the electronic structure of Y_2C. Because the secondary electron cutoff from the higher energy is screened by the cutoff from the lowest one,[30] we conclude that the observed low value of $\Phi_{WF,poly}$ originates from the $(11\bar{2}0)_H$ surfaces. Furthermore, the $\Phi_{WF,poly}$ of Y_2C was reduced compared with that of yttrium metal (3.1 eV).[31] Such a low $\Phi_{WF,poly}$ reveals the loose bound character of delocalized electrons in Y_2C.

Electronic Structure. The experimental results illustrate that Y_2C has a layered structure that is similar to that of Ca_2N. The band structures of these compounds consist of a valence band that is occupied by the loose electrons at the interstitial sites.[16] In contrast to the half-occupied valence band in Ca_2N, the valence band in Y_2C is almost fully occupied, and the E_F is lifted to the top of the band; in this way, a small number of electrons are transferred into the higher-energy band through a slightly indirect overlap between these two bands (Figure 4a). The lower energy band (the blue line) serves as a hole-like band, while the higher-energy band (the red line) serves as an electron-like band, corresponding to the two cylinder-like Fermi surfaces. The cylinder-like Fermi surfaces with a slight distortion along the c-axis result in Y_2C with a quasi-2D character (Figure 4c). Figure 4b depicts the total and projected DOSs (PDOSs). The total DOS at E_F ($N_{tot}(E_F)$) is 3.27 states/eV f.u., which is close to but slightly smaller than the experimental $N(E_F)$ of 3.95 states/eV f.u. This result could be due to the electron−phonon coupling, which enhances the $N(E_F)$ by a factor of $1 + \lambda = 1.21$, where λ is the electron−phonon coupling constant ($\lambda = 0.21$). The total DOS representing excess electrons near the E_F is energetically separated from the rest of the underlying occupied bands. The $N_{tot}(E_F)$ is mainly built from the interstitial states around the X sites and the Y 4d-states, which is quite different from the case of Ca_2N, where the $N(E_F)$ for Ca_2N mainly consists of the interstitial states around the X sites.[12] Figure 4d shows the total valence electron density and the partial electron density (PED) averaged over the hexagonal ab plane (perpendicular to the c-axis). The valence electrons (black line) are distributed mainly around the ion sites and within the cationic slab, while the electrons within k_BT of the E_F (i.e., $|E - E_F| < 0.025$ eV) are mainly confined between the neighboring cationic slabs, where the peaks evenly across the interlayer space and extends partly into the cationic layers. The electron density map of the $(11\bar{2}0)_H$ plane (Figure 4e) shows that the electrons near the E_F do not distribute uniformly, but locate within ellipsoidal regions around the X sites. The ellipsoidal electron density distribution around X is rather inhomogeneous, and the long axis of the ellipsoid extends into the cationic layers, which is consistent with the results of PED. Bonding analysis based on the ELF suggests that the bondings between Y, C, and the anionic electron around X are mainly ionic (Figure 4f). All results obtained by the DFT calculations reveal that there are electrons confined in the interlayer space stoichiometrically, serving as anions, and the electronic structure of Y_2C has a quasi-2D character. Thus, Y_2C can be regarded as a quasi-2D electride.

■ DISCUSSION

Because of the band filling induced by raising the E_F, the Fermi surfaces locate at Brillouin zone (BZ) boundaries (the BA and FL lines for the hole-like and electron-like bands, respectively, see Figure 4c), not centered at the origin of BZ (Γ−Z line) as they are in Ca_2N. This, in turn, leads to the remarkable decrease of $N(E_F)$, resulting in the lower conductivity and much lower carrier concentration in Y_2C. The calculated carrier numbers per f.u. are 0.19 holes and 0.19 electrons, according to the equation $N = 2(1/8)V_F/V_k$, where V_F is the volume within the calculated Fermi surface and V_k is the volume of one k-state.

dx.doi.org/10.1021/cm503512h | Chem. Mater. 2014, 26, 6638−6643

The almost-equal hole and electron densities suggest serious carrier compensation in Y_2C, which explains the linear field-dependence of $\rho_{xy}(T,H)$ and supports that Y_2C behaves as a semimetal. With the above N values, one can roughly estimate the m^* of hole (or electron) by an almost-free electron assumption and the equation $m^* = (3h^3N/8\pi)^{2/3}/2E$, where E is the difference between the E_F and electron-like band minimum (or the difference between the hole-like band maximum and the E_F). The estimated m^* is $8.4m_0$ for the hole and $5.1m_0$ for the electron. According to the enhancement of $N(E_F)$ observed by heat capacity measurement ($1+\lambda = 1.21$), the thermal m^* should be 1.21 times larger than the estimated values ($10.2m_0$ for the hole and $6.2m_0$ for the electron). They are comparable to the m^* determined from n_0 and γ data. It undoubtedly indicates that the m^* of Y_2C is much larger than that of Ca_2N. The total charge of each individual atom is calculated by integrating the PDOSs up to the E_F, and the results are summarized in Table 1. It can be seen that the numbers of 4d and 5s electrons at the Y site are 0.928 and 0.144, respectively, indicating that the electrons delocalized at the X site are mainly transferred from the 5s electron of Y. Since the total charge of Y is +7.065, the valence state of Y is +1.935. On the other hand, most of the electrons transferred to C are located in the 2p band, and the calculated valence state of C is −2.043. Because of the requirement of charge neutrality, the valence state of X is −1.827. The result that the number of electrons at the X site is less than 2 per unit cell indicates that the electrons confined in the interlayer space do not behave like almost-free electrons as in Ca_2N, and the bonds in the X site and cationic slab are ionic with a partial covalent character. Therefore, the chemical formula of Y_2C can be expressed as $[Y_2^{1.9+}C^{2-}]\cdot 1.8e^-$. In addition, the existence of a localized 4d electron at the Y site is confirmed by the fitted μ_{eff} from the χ−T curve, using the modified Curie−Weiss law. The value of μ_{eff} is smaller than that of Y^{2+}, considering one localized d-electron at the Y site (1.73 μ_B/Y), which can be ascribed to itinerancy of the electrons and the hybridization between Y and C, as well as the orbitals at X sites. On the other hand, the strong hybridization between the interstitial states around the X sites and the Y 4d-states leads to the deviation of the band structure from parabolic type, such as the flat parts along the Γ−L and Z−F lines. The bands flattening near E_F are the origin of the large m^* of Y_2C.

Table 1. Electron Counts on the Constituent Orbitals (Total and Transferred Charges Are Shown for Each Ion in Y_2C)

element	s	p	d	total	transferred
Y	0.144	5.993	0.928	7.065	−1.935
C	1.816	3.964	0.263	6.043	+2.043
X[a]				1.827	+1.827

[a]The interstitial site between Y_2C layers.

■ CONCLUSIONS

To summarize, our experimental and theoretical results suggest that Y_2C is a quasi-two-dimensional (quasi-2D) electride with a chemical formula of $[Y_2C]^{1.8+}\cdot 1.8e^-$. This is the first example of an electride that contains transition-metal elements with valence d-electrons. The introduction of the localized d-orbitals to the anionic electron in Y_2C changes the relative contribution of the localized orbital to the orbital at interstitial sites. With this clue, we realized the evolution from the almost-free electron-like 2D electride Ca_2N to the semimetal-like quasi-2D electride Y_2C with heavy carriers using electronic structure design. The current study will not only expand our scope of inorganic electrides, but also promote the development of practical applications.

■ AUTHOR INFORMATION

Corresponding Author

*E-mail: hosono@msl.titech.ac.jp.

Author Contributions

¶X.Z. and Z.X. contributed equally.

Notes

The authors declare no competing financial interest.

■ ACKNOWLEDGMENTS

This work was supported by the JST ACCEL Program and MEXT Elements Strategy Initiative to Form Core Research Center. The HAXPES measurements were performed with approval of the NIMS Synchrotron X-ray Station (Proposal Nos. 2013A4715, 2013B4703, and 2014A4700). S.U. is grateful to HiSOR, Hiroshima University, and JAEA/SPring-8 for the development of HAXPES at BL15XU.

■ REFERENCES

(1) Dye, J. L. *Acc. Chem. Res.* **2009**, *42*, 1564−1572.
(2) Dye, J. L. *Science* **2003**, *301*, 607−608.
(3) Matsuishi, S.; Toda, Y.; Masashi, M.; Katsuro, H.; Toshio, K.; Hirano, M.; Tanaka, I.; Hosono, H. *Science* **2003**, *301*, 626−629.
(4) Kim, S. W.; Shimoyama, T.; Hosono, H. *Science* **2011**, *333*, 71−74.
(5) Toda, Y.; Yanagi, H.; Ikenaga, E.; Kim, J. J.; Kobata, M.; Ueda, S.; Kamiya, T.; Hirano, M.; Kobayashi, K.; Hosono, H. *Adv. Mater.* **2007**, *19*, 3564−3569.
(6) Xu, H. L.; Li, Z. R.; Wu, D.; Wang, B. Q.; Li, Y.; Gu, F. L.; Aoki, Y. *J. Am. Chem. Soc.* **2007**, *129*, 2967−2970.
(7) Ellaboudy, A.; Dye, J. L.; Smith, P. B. *J. Am. Chem. Soc.* **1983**, *105*, 6490−6491.
(8) Dale, S. G.; Otero-de-la-Roza, A.; Johnson, E. R. *Phys. Chem. Chem. Phys.* **2014**, *16*, 14584−14593.
(9) Ichimura, A. S.; Dye, J. L.; Camblor, M. A.; Villaescusa, L. A. *J. Am. Chem. Soc.* **2002**, *124*, 1170−1171.
(10) Kim, K. B.; Kikuchi, M.; Miyakawa, M.; Yanagi, H.; Kamiya, T.; Hirano, M.; Hosono, H. *J. Phys. Chem. C* **2007**, *111*, 8403−8406.
(11) Kitano, M.; Inoue, Y.; Yamazaki, Y.; Hayashi, F.; Kanbara, S.; Matsuishi, S.; Yokoyama, T.; Kim, S. W.; Hara, M.; Hosono, H. *Nat. Chem.* **2012**, *4*, 934−940.
(12) Lee, K.; Kim, S. W.; Toda, Y.; Matsuishi, S.; Hosono, H. *Nature* **2013**, *494*, 336−340.
(13) Ma, Y.; Eremets, M.; Oganov, A. R.; Xie, Y.; Trojan, I.; Medvedev, S.; Lyakhov, A. O.; Valle, M.; Prakapenka, V. *Nature* **2009**, *458*, 182−183.
(14) Pickard, C. J.; Needs, R. J. *Nat. Mater.* **2010**, *9*, 624−627.
(15) Miao, M. S.; Hoffmann, R. *Acc. Chem. Res.* **2014**, *47*, 1311−1317.
(16) Inoshita, T.; Jeong, S.; Hamada, N.; Hosono, H. *Phys. Rev. X* **2014**, *4*, 031023.
(17) TOPAS, Version 4.2, Bruker AXS: Karlsruhe, Germany, 2009.
(18) Ueda, S.; Katsuya, Y.; Tanaka, M.; Yoshikawa, H.; Yamashita, Y.; Ishimaru, S.; Matsushita, Y.; Kobayashi, K. *AIP Conf. Proc.* **2010**, *1234*, 403−406.
(19) Ueda, A. S. *J. Electron Spectrosc. Relat. Phenom.* **2013**, *190*, 235−241.
(20) Perdew, J. P.; Burke, K.; Ernzerhof, M. *Phys. Rev. Lett.* **1996**, *77*, 3865−3868.
(21) Kresse, G.; Furthmüller, J. *Phys. Rev. B* **1996**, *54*, 11169−11186.

(22) Blaha, P.; Schwarz, K.; Madsen, G. K. H.; Kvasnicka, D.; Luitz, J. *WIEN2k*; Technische Universität Wien: Vienna, Austria, 2011.
(23) Kokalj, A. *Comput. Mater. Sci.* **2003**, *28*, 155−168.
(24) Uijttewaal, M. A.; de Wijs, G. A.; de Groot, R. A. *J. Appl. Phys.* **2004**, *96*, 1751−1753.
(25) Atoji, M.; Kikuchi, M. *J. Chem. Phys.* **1969**, *51*, 3863−3872.
(26) Hall, P. M.; Legvold, S.; Spedding, F. H. *Phys. Rev.* **1959**, *116*, 1446−1447.
(27) Arajs, S.; Colvin, R. V. *J. Less-Common. Met.* **1962**, *4*, 572−578.
(28) Chambers, R. G. *Proc. Phys. Soc. A* **1952**, *65*, 903−910.
(29) Chechernikov, V. I.; Pop, I.; Terekhova, V. F.; Kolesnichenko, V. E. *Sov. Phys.—JETP* **1964**, *19*, 298−299.
(30) Grepstad, J. K.; Gartland, P. O.; Slagsvold, B. *Surf. Sci.* **1976**, *57*, 348−362.
(31) Eastman, D. E. *Phys. Rev. B* **1970**, *2*, 1−2.